Lecture Notes in Applied and Computational Mechanics 96

Michael Kaliske · Markus Oeser ·
Lutz Eckstein · Sabine Leischner ·
Wolfram Ressel ·
Frohmut Wellner *Editors*

Coupled System Pavement—Tire—Vehicle

A Holistic Computational Approach

Springer

Lecture Notes in Applied and Computational Mechanics

Volume 96

Series Editors

Peter Wriggers, Institut für Kontinuumsmechanik, Leibniz Universität Hannover, Hannover, Niedersachsen, Germany

Peter Eberhard, Institute of Engineering and Computational Mechanics, University of Stuttgart, Stuttgart, Germany

This series aims to report new developments in applied and computational mechanics - quickly, informally and at a high level. This includes the fields of fluid, solid and structural mechanics, dynamics and control, and related disciplines. The applied methods can be of analytical, numerical and computational nature. The series scope includes monographs, professional books, selected contributions from specialized conferences or workshops, edited volumes, as well as outstanding advanced textbooks.

Indexed by EI-Compendex, SCOPUS, Zentralblatt Math, Ulrich's, Current Mathematical Publications, Mathematical Reviews and MetaPress.

More information about this series at http://www.springer.com/series/4623

Michael Kaliske · Markus Oeser · Lutz Eckstein ·
Sabine Leischner · Wolfram Ressel ·
Frohmut Wellner
Editors

Coupled System Pavement—Tire—Vehicle

A Holistic Computational Approach

Springer

Editors
Michael Kaliske
Institute for Structural Analysis
TU Dresden
Dresden, Germany

Lutz Eckstein
Institute for Automotive Engineering
RWTH Aachen University
Aachen, Germany

Wolfram Ressel
Institute for Road and Transport Science
University of Stuttgart
Stuttgart, Germany

Markus Oeser
Institute of Highway Engineering
RWTH Aachen University
Aachen, Germany

Sabine Leischner
Institute of Urban and Pavement
Engineering
TU Dresden
Dresden, Germany

Frohmut Wellner
Institute of Urban and Pavement
Engineering
TU Dresden
Dresden, Germany

ISSN 1613-7736 ISSN 1860-0816 (electronic)
Lecture Notes in Applied and Computational Mechanics
ISBN 978-3-030-75485-3 ISBN 978-3-030-75486-0 (eBook)
https://doi.org/10.1007/978-3-030-75486-0

© The Editor(s) (if applicable) and The Author(s), under exclusive license to Springer Nature Switzerland AG 2021
This work is subject to copyright. All rights are solely and exclusively licensed by the Publisher, whether the whole or part of the material is concerned, specifically the rights of translation, reprinting, reuse of illustrations, recitation, broadcasting, reproduction on microfilms or in any other physical way, and transmission or information storage and retrieval, electronic adaptation, computer software, or by similar or dissimilar methodology now known or hereafter developed.
The use of general descriptive names, registered names, trademarks, service marks, etc. in this publication does not imply, even in the absence of a specific statement, that such names are exempt from the relevant protective laws and regulations and therefore free for general use.
The publisher, the authors and the editors are safe to assume that the advice and information in this book are believed to be true and accurate at the date of publication. Neither the publisher nor the authors or the editors give a warranty, expressed or implied, with respect to the material contained herein or for any errors or omissions that may have been made. The publisher remains neutral with regard to jurisdictional claims in published maps and institutional affiliations.

This Springer imprint is published by the registered company Springer Nature Switzerland AG
The registered company address is: Gewerbestrasse 11, 6330 Cham, Switzerland

Preface

Road infrastructure is essential for the establishment and maintenance of competitive and successful industrialized societies. Further, infrastructural investments represent a huge economic value. While the development of new vehicles and intelligent transportation concepts in Germany is primarily driven by industry, there have not been significant innovations in the field of pavement structures in recent decades. This deficit originates from two sources. First, this research lacks research funds that—in contrast to commercial automotive products—are supplied predominantly by public resources. Second, relatively strict and inflexible regulations hinder creativity, the transfer of knowledge, and the innovative capacity of German industry, engineers, and scientists. These circumstances contribute to the fact that so far, the approaches of progressive engineering sciences in the construction and maintenance of pavement infrastructures have not or have rarely been used. Consequently, current solutions are often inadequate and lack durability.

To overcome this problem and to prepare road infrastructure for future requirements, a paradigm shift towards dimensioning, structural realization, and the maintenance of pavements is needed. Research Unit FOR 2089, funded by the German Research Foundation (DFG), aimed to develop the scientific base for this shift. The main goal of Research Unit FOR 2089 is to provide a coupled thermo-mechanical model for a holistic physical analysis of the pavement-tire-vehicle system. Based on this model, pavement structures and materials can be optimized so that new demands become compatible with the main goal—durability of the structures and the materials.

The development of the scientific base for these new and qualitatively improved modeling approaches requires a holistic procedure through the coupling of theoretical numerical and experimental approaches as well as an interdisciplinary and closely linked handling of the coupled pavement-tire-vehicle system. This interdisciplinary research provided a deeper understanding of the physics of the full system through complex, coupled simulation approaches and progress in terms of improved, and therefore, more durable and sustainable structures.

The inter-and multi-disciplinary research required to approach the challenging topics to be addressed by Research Unit FOR 2089 has been carried out by five closely linked sub-projects carried out at the Institute for Structural Analysis (TU Dresden), the Institute of Highway Engineering (RWTH Aachen), the Institute for

Road and Transport Science (University of Stuttgart), the Institute of Urban and Pavement Engineering (TU Dresden), and the Institute for Automotive Engineering (RWTH Aachen).

All reported contributions in this book are outcomes of Research Unit FOR 2089. The financial support of the German Research Foundation is gratefully acknowledged.

Dresden, Germany — Michael Kaliske
Aachen, Germany — Markus Oeser
April 2021

Contents

Multi-physical and Multi-scale Theoretical-Numerical Modeling of Tire-Pavement Interaction

Michael Kaliske, Ronny Behnke, Felix Hartung, and Ines Wollny

Abstract In this chapter, the tire-pavement system as one subsystem of the complex vehicle-tire-pavement system is investigated in detail. As basic framework, the finite element method (FEM) is used for both, tire and pavement simulation, to obtain a detailed representation of the dynamic system, where the special case of steady state motion of the rolling tire is considered. The finite element (FE) discretization further enables to study the tire-pavement interface in terms of transmitted stresses and friction characteristics for different tire and surface properties. For the modeling of this complex subsystem, new FE based analysis methods have been derived using the Arbitrary Lagrangian-Eulerian (ALE) framework for tire and pavement. With the help of the ALE framework, the relative motion of tire and pavement is captured in a computationally efficient way. Friction in the tire-pavement interface is numerically represented by a homogenization approach of the friction interface over several length scales. With the help of a time homogenization technique, spatially detailed long-term predictions regarding rutting of the pavement become feasible by considering different time scales of the thermo-mechanical investigation.

Keywords Tire · Pavement · Interaction · Friction · Simulation · Prediction

1 Introduction

As part of our infrastructure, the road network (Fig. 1) fulfills several important functions to guarantee our today's road-bound mobility. During the last decades, new fundamental developments of the automobile population took place and, at the moment, a further transformation from fossil-fuel-powered vehicles to electrically driven vehicles is expected. Regarding the pavement structure, less innovations in

Funded by the German Research Foundation (DFG) under grant KA 1163/30.

M. Kaliske (✉) · R. Behnke · F. Hartung · I. Wollny
Institute for Structural Analysis, Technische Universität Dresden, Dresden, Germany
e-mail: michael.kaliske@tu-dresden.de

© The Author(s), under exclusive license to Springer Nature Switzerland AG 2021

M. Kaliske et al. (eds.), *Coupled System Pavement—Tire—Vehicle*,
Lecture Notes in Applied and Computational Mechanics 96,
https://doi.org/10.1007/978-3-030-75486-0_1

Fig. 1 Road network in Germany, motorway A4 (Dresden)

terms of new materials or construction principles can be observed. To stimulate fundamental developments of new pavement structures and to increase their durability/performance [1, 26, 29, 39, 48], new numerical methods have been proposed for a holistic analysis of the vehicle-tire-pavement system [20] to understand the underlying basic interaction principles within a larger system approach.

The research presented in this chapter was conducted within a subproject of the Research Unit FOR 2089 "Durable Pavement Constructions for Future Traffic Loads: Coupled System Pavement-Tire-Vehicle" funded by the German Research Foundation (DFG). In this subproject and the present chapter, the tire-pavement subsystem is analyzed in more detail, see Fig. 2. Here, the tire-pavement interaction plays an important role for the handling and safety of the vehicles [16, 18] but also for the correct assessment of the mechanical loading of the pavement [22, 38].

The objective is to propose a numerically efficient continuum mechanical macroscopic and thermo-mechanical finite element (FE) formulation of the coupled tire-pavement model based on a stationary Arbitrary Lagrangian-Eulerian (ALE) formulation for both, tire and pavement. The consistently coupled models consist of an inelastic thermo-mechanical ALE FE tire model, a homogenized friction model considering different length scales of the friction surface and an inelastic thermo-mechanical ALE FE pavement model. This global FE approach enables to study the deformation of tire and pavement at steady state rolling contact. Macroscopic material parameters for the asphalt materials are identified based on experimental tests presented in chapter "Experimental Methods for the Mechanical Characterization of Asphalt Concrete at Different Length Scales: Bitumen, Mastic, Mortar and Asphalt Mixture".

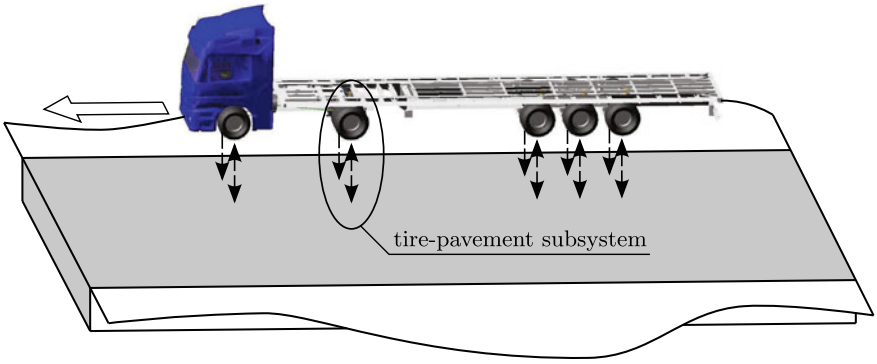

Fig. 2 Vehicle-tire-pavement system with tire-pavement subsystem (tire, tire-pavement interface with friction characteristics and pavement)

The thermo-mechanical contact formulation uses the numerical framework of a multi-scale friction analysis. In this framework, a general macroscopic friction law considering the frictional effects of hysteresis and adhesion of the contacting partners (rubber and pavement surface) at different length scales is obtained by numerical homogenization. A comparison of this friction model to friction tests is included in chapter "Numerical Friction Models Compared to Experiments on Real and Artificial Surfaces".

Special attention is paid in the present chapter to the numerical modeling and assessment of long-term processes of the pavement subjected to rolling traffic load and changing temperature conditions (climate). The numerically efficient treatment of the long-term processes influencing the durability of the pavement structure (i.e. rut formation) is accomplished by a temporal multi-scale formulation of the tire-pavement system. With the help of a time homogenization technique, repeated mechanical impact on the pavement (passing of tires) in the short term as well as climate effects (varying temperature fields due to day-night change, seasonal change) in the long term are computed to assess the consequences for tire and pavement.

A coupling of the macroscopic pavement model to a microscopic asphalt model is shown in chapter "Multi-scale Computational Approaches for Asphalt Pavements under Rolling Tire Load". The models presented in this chapter are, further, included in chapter "Simulation Chain: From the Material Behavior to the Thermo-mechanical Long-term Response of Asphalt Pavements and the Alteration of Functional Properties (Surface Drainage)" to obtain an overall coupled simulation approach.

Outline. In Sect. 2, the FE discretized tire model and the thermo-mechanical framework for its analysis at steady state rolling are introduced. In Sect. 3, friction in the tire-pavement interface is assessed by a developed numerical framework of multi-scale friction analysis. The loading of the inelastic and deformable pavement structure by rolling tires is then investigated in Sect. 4. Here, the ALE FE pavement model for short-term loading is introduced for thermo-mechanical analysis. In Sect. 5, the

afore-discussed submodels are combined to study tire-pavement interaction phenomena. In Sect. 6, a computationally efficient method for the long-term analysis of the pavement structure is presented and discussed. A conclusion and outlook of the chapter is given in Sect. 7.

2 Tire Model

In Fig. 3, different approaches to represent the tire within a numerical simulation are illustrated. While simplified rheological models with a reduced set of degrees of freedom (DOF) are mainly employed in analytical vehicle simulations, more detailed information on the tire response can be obtained by the belt-spring tire model used in multi-body simulations of vehicles driving on a flat or uneven surface (see chapter "Experimental and Simulative Methods for the Analysis of Vehicle-Tire-Pavement Interaction") or via an FE discretized tire model. However, in the latter cases, the number of DOF and the computational effort increase. Hence, detailed information regarding the tire contact patch or the tire structure itself might be expected by an FE model of the tire, but normally, the computational effort of an FE discretized model for a dynamic tire simulation is too high.

2.1 Thermo-mechanical FE Tire Model

In order to obtain a detailed FE representation of the tire at low computational cost, an inelastic ALE FE approach has been developed and applied to the tire models used in this study. The ALE FE approach allows to reduce the DOF of the tire

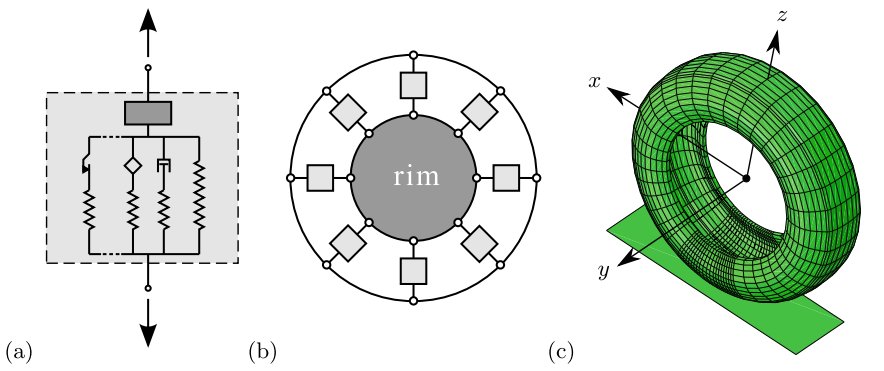

Fig. 3 Different approaches for the numerical representation of the tire within the tire-pavement system: **a** 1-mass model with reduced rheology, **b** belt-spring models with simplified rubber ring, tread stiffness and rigid rim, **c** full 3D FE model of the tire, see [10]

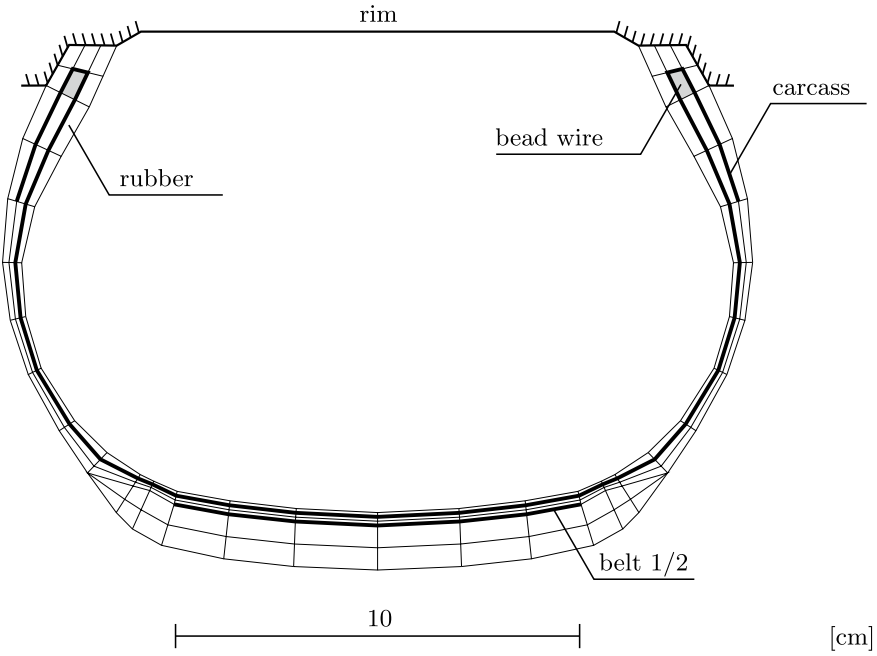

Fig. 4 FE discretized cross-section of the 175 SR 14 passenger car tire (PCT) used as benchmark tire, see [6] (carcass layer with polyethylene terephthalate (PET) cords)

since only the contact region of the tire requires a finer discretization by FE and the motion of the tire (rolling) is represented by flow of the material through the fixed FE mesh of the tire structure rather than using the tire as a moving body/load in a transient framework [11]. In [5], the procedure is described for the incorporation of inelastic effects stemming from dissipative rubber compounds. In the following, a brief overview of the methodology is provided.

In Fig. 4, the cross-section of the tire model used for benchmark tests in the further analyses is shown. Additional information on the discretization in circumferential direction and the components/material characteristics of the simple passenger car tire (PCT) is available in [6]. For the rubber compounds and cords, nonlinear material models have been developed and used to obtain a thermo-mechanical description of the tire structure at large strains. For dimensioning-relevant tire-pavement configurations, different FE discretized truck tire models are employed.

For its thermo-mechanical analysis at steady state rolling, a sequentially coupled, modular analysis scheme has been implemented, see Fig. 5. The analysis consists of a mechanical module and a thermal module. In the mechanical module, the energy dissipation stemming from the inelastic (i.e. viscoelastic) rubber compounds is computed from the current steady state motion of the rolling tire at fixed cross-sectional temperature profile. The cross-sectional temperature profile of the tire is then computed and updated via the current information on the dissipated energy of cross-

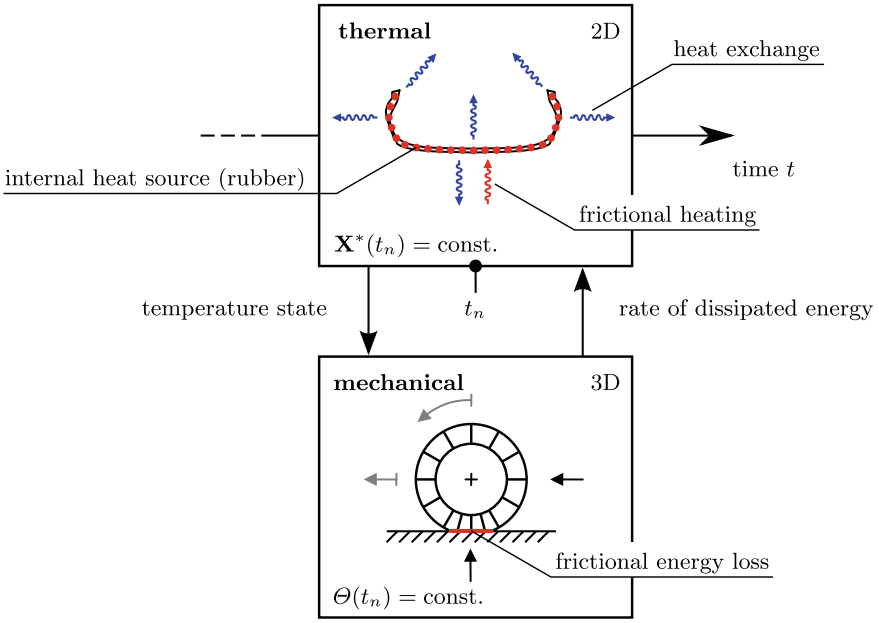

Fig. 5 Sequentially coupled thermo-mechanical simulation approach for the thermo-mechanical investigation of steady state rolling inelastic tires, see [5]

sectional points of the tire. The method is described in detail in [5], where different tires have been analyzed at different rolling conditions. Special attention has been paid to the correct implementation of thermal boundary conditions as a function of the temperature of the environment (air, road) [35]. Infrared surface temperature measurements of the rotating tire have been carried out on a drum test rig to validate the developed simulation strategy, see [5].

From the dissipated energy at rolling, the rolling resistance of the tire is computed by the sequentially coupled simulation approach as a function of the elapsing time and the current temperature state of the tire. Due to the incorporation of inelastic effects within the mechanical simulation of the tire, the rolling resistance can be obtained as reaction force or moment as a direct outcome of the tire simulation or as an integrated quantity from an energetic approach. These different procedures are described in more detail in [5].

3 Friction

Friction (defined as force resisting the relative motion of solid surfaces, fluid layers and material elements sliding against each other) is a complex phenomenon and has significant importance in daily life. This challenging field of research is also associated with tire industry, because tire-pavement interaction affects every driving

maneuver. Friction in general consists of different contributions: hysteresis, adhesion as well as viscous friction and interlocking effects. Hysteresis friction due to internal dissipation of the viscoelastic material and adhesion friction in consequence of molecular bonding to the surface represent the main friction contributions. Adhesion as well as hysteresis friction strongly depend on e.g. contact pressure, sliding velocity and temperature conditions. In Sect. 3.1, an adhesion model is introduced which can be coupled to a developed multi-scale approach for hysteresis friction (see Sect. 3.2).

3.1 Adhesion Friction

Adhesion in contrast to cohesion mainly describes the molecular bonds between two different surfaces. The debonding process can also be called decohesion between two different materials [46]. In the FEM, adhesion friction can e.g. be modeled by a nonlinear traction-separation-law with the adhesional stress vector

$$\boldsymbol{\sigma} = (1 - D) \cdot K \cdot \boldsymbol{\delta} \tag{1}$$

that is a function of the relative separation vector $\boldsymbol{\delta}$ between two contact points in normal and two tangential directions, the initial adhesional stiffness K and the damage function D. The evolution of damage is comparable to the devolution of the intensity of adhesion proposed in [32]. Different analytical functions to describe the evolution of the damage value, e.g. a bilinear formulation, can be used. A nonlinear approach

$$D = \frac{G}{G_{\text{tot}}} = \frac{1}{G_{\text{tot}}} \int_0^{\delta_{\max}} \hat{\sigma} \, \mathrm{d}\delta \tag{2}$$

with only two unknown parameters (K, G_{tot}) is chosen to decrease the numerical effort of parameter identification. As soon as the damage value is zero, no stresses can be transferred between the contact points (total debonding). In Eq. (2), G and G_{tot} represent the current and total fracture energy (corresponds to the area underneath the transferred stress, see Fig. 6), whereas $\delta_{\max} = \max(\|\boldsymbol{\delta}\|)$ is the largest separation and $\hat{\sigma} = \|\boldsymbol{\sigma}\|$ stands for the absolute adhesion stress.

The adhesion model distinguishes between normal (without contact) and tangential adhesion (with contact). Therefore, only one damage value is required to characterize transmitted stresses. The damage value described in Eq. (2) is reset to zero (healing) as soon as the fracture energy is reached in normal direction. After the points come into contact again (bonding), damage can evolve repeatedly due to further tangential or normal separation. For some scenarios (e.g. remaining stress transmission after $D = 1$), it is suitable to ensure minimal friction after tangential debonding. Therefore, a classical Coulomb law (represented by $\mu_{\text{adh},0}$) is added to the adhesion model via hyperbolic tangent regularization, see [46].

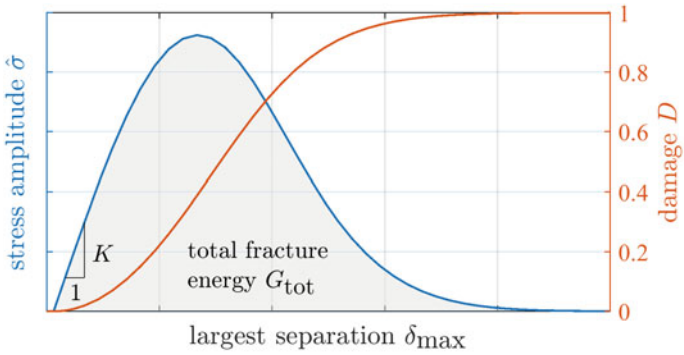

Fig. 6 Traction-separation-law of adhesion model

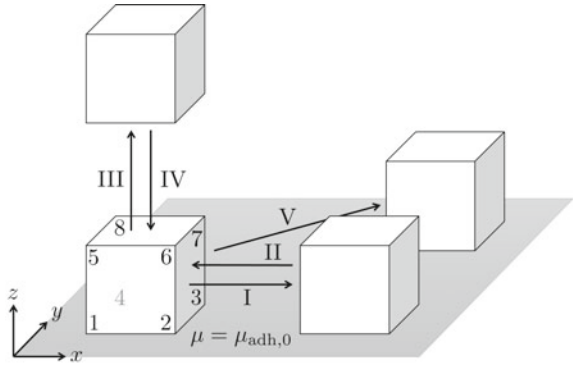

Fig. 7 Patch test for adhesion model

A patch test to represent the functionality of the adhesion model is shown in Fig. 7 that is comparable to [47]. There, a cube with edge length of 1 mm is pressed by $1\,{}^{\text{N}}/_{\text{mm}^2}$ on a rigid surface. Then, the upper nodes (5–8) are moved 0.1 mm along the x-axis (Step I). In the second step, the same nodes are moved back to the original position. Then the upper nodes are lifted up 0.1 mm along the z-axis (Step III). Within Step IV, the cube is moved back to its initial position. Finally, all upper block nodes are shifted diagonally (0.1 mm in x-direction and 0.1 mm in y-direction). The duration of each step is one second. The bottom nodes (1–4) are coupled in z-direction to avoid tipping which could occur at high shear forces. The initial adhesion stiffness K is set to $100\,{}^{\text{N}}/_{\text{mm}^3}$ and the total fracture energy G_{tot} is $0.01\,{}^{\text{N}}/_{\text{mm}}$. The additional Coulomb friction coefficient to characterize friction between the cube and the rigid surface is $\mu_{\text{adh},0} = 0.5$.

The damage value D of Node 1 (identical to Nodes 2–4 due to coupling in z-direction) as well as the reaction forces of the rigid body surface are shown in Fig. 8. During the first step, the adhesion stress (only in first tangential direction) is observed until the total fracture energy is reached. As soon as D is equal to zero, only shear stresses due to Coulomb friction are transmitted. The shear stress changes the sign

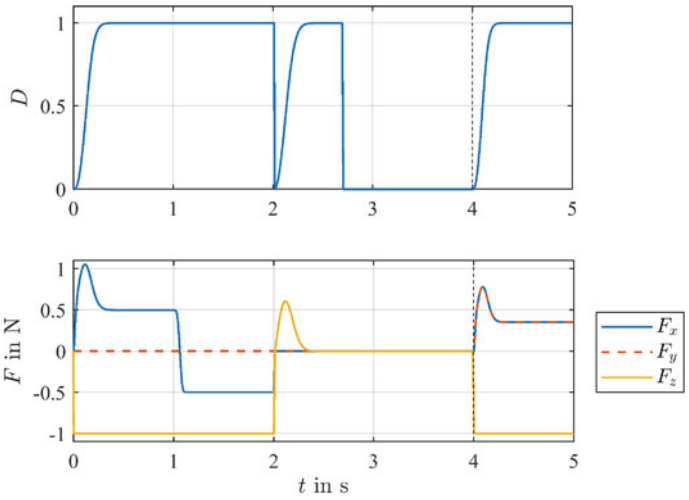

Fig. 8 Damage values and reaction forces during the patch test

while moving back in Step II. In the third step, the adhesion stress in normal direction is activated. Since the bottom nodes of the cube are in contact with the counter surface at the end of Step IV again, adhesion stresses as well as Coulomb friction in both tangential directions appear in the final Step V. Note that the peaks of the adhesion stresses in Step V are lower than in Step I and III, because there is separation in more than one direction. Moreover, the total fracture energy G_{tot} is reached earlier.

Further developments, e.g. usage of different initial adhesion stiffness parameters for normal and tangential adhesion, would be conceivable, but also include increased complexity regarding parameter identification.

3.2 Hysteresis Friction

The so-called hysteresis effect is a consequence of the internal dissipation of the viscoelastic material of e.g. rubber. Hence, the substrate structure is characterized by many asperities and it is important to understand the physical background of hysteresis friction on different length scales. The analytical approaches for multi-scale friction of Persson (see among others [31]) and [23] are common and show suitable results compared to friction measurements. Numerical models like the multi-scale approaches [14, 17, 36, 47], which base for instance on the FEM, give the opportunity to consider additional multi-physical phenomena. In the following part, a scale identification method and homogenization for hysteresis friction are introduced to build up a multi-scale friction approach which is validated numerically.

Scale Identification. Due to the different asperities of a rough surface, e.g. asphalt pavement, it is necessary to consider the entire frequency spectrum or length scales. The height difference correlation function (HDCF)

$$C_{\mathrm{HDC}}(\zeta) = \left\langle (z(x+\zeta) - z(x))^2 \right\rangle, \tag{3}$$

which compares the height z of two points with the distance ζ, is one method to characterize a multi-scale surface texture (compare [14, 47]). The brackets $\langle \ldots \rangle$ in Eq. (3) denote the mean value of the expression associated with. By applying e.g. sine waves to describe the surface on each length scale analytically, an approximation of the HDCF

$$\begin{aligned} \tilde{C}_{\mathrm{HDC}}(\zeta) &= \sum_{i=1}^{n} \frac{B_i}{\pi} \int_0^{\pi/B_i} \left[A_i \sin(B_i x + B_i \zeta) - A_i \sin(B_i x)\right]^2 \mathrm{d}x \\ &= \sum_{i=1}^{n} 2 A_i^2 \sin^2\left(\frac{B_i \zeta}{2}\right) \end{aligned} \tag{4}$$

can be used to identify the sine wave parameters A_i and B_i within a fitting algorithm explained in [17]. Other surface characterization methods like the power spectral density function proposed in [36] or bandpass filters introduced in [37] are also applied in multi-scale rubber friction models.

Friction Homogenization and Scale-Dependent Friction Law. Friction features on a specific length scale can be homogenized to generate friction characteristics for a next coarser length scale. For this purpose, FE simulations are performed on the block level. During every simulation, a rubber block is pressed on a periodic rigid surface that is generated by the scale identification algorithm. The block length is identical to the current wave length λ_i. Then, the block is sliding over the rough rigid surface with a constant velocity. Periodic boundary conditions at the leading and trailing block edge are applied. The top nodes of the block are coupled in z-direction to ensure uniform vertical displacements. Temperature evolution is neglected within the FE simulation. The ratio of the total horizontal and vertical reaction forces forms the friction coefficient $\mu_{\mathrm{hyst}}(t)$ as a function of time. A time homogenization algorithm of the friction coefficient

$$\mu_{\mathrm{hyst,hom}} = \frac{1}{t_{\mathrm{tot}} - t_{\mathrm{st}}} \int_{t_{\mathrm{st}}}^{t_{\mathrm{tot}}} \mu_{\mathrm{hyst}}(t)\, \mathrm{d}t \tag{5}$$

is introduced to take only the steady state part, starting at $t = t_{\mathrm{st}}$, into account. Via an abort criterion

$$Q \leq \left| 1 - \frac{\bar{\mu}_{\mathrm{hyst},k}}{\bar{\mu}_{\mathrm{hyst},k-1}} \right| \tag{6}$$

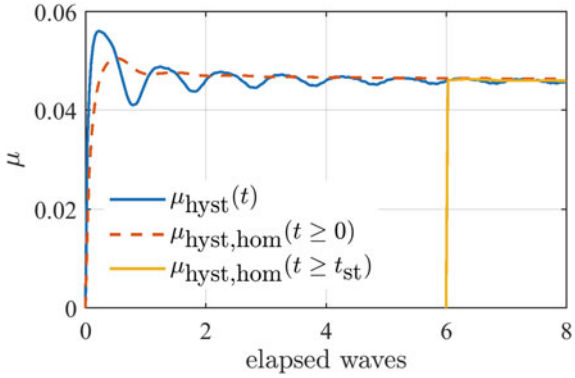

Fig. 9 Time homogenization of the friction coefficient

with

$$\bar{\mu}_{\text{hyst,k}} = \frac{v}{\lambda} \int_{(k-1)\cdot\frac{\lambda}{v}}^{k\cdot\frac{\lambda}{v}} \mu_{\text{hyst}}(t)\,\mathrm{d}t\,, \tag{7}$$

the steady state time $t_{\text{st}} = k \cdot \lambda/v$ is defined. The required height and discretization of the rubber block as well as the time in which the imposed pressure is applied influence the friction coefficient significantly and need to be identified within a parameter study [12]. In Eq. (7), parameter λ represents the current wave length and k stands for the number of elapsed waves. In Fig. 9, t_{st} is reached after six periods. A friction law for the next upper scale is created by piecewise cubic spline interpolation

$$\mu_{\text{hyst,spl}}(p, v) = \sum_{i=1}^{n_p} \sum_{j=1}^{n_v} c_{i,j} \cdot \left(p - \xi_p\right)^{n_p - i} \cdot (v - \xi_v)^{n_v - j} \tag{8}$$

with $n_p = n_v = 4$ (cubic spline generation), the breakpoints ξ_p and ξ_v (load and velocity conditions in each block simulation) and the spline coefficients $c_{i,j}$. Figure 10 shows the homogenized friction coefficients (red dots) at breakpoints ξ_p and ξ_v as well as the spline evaluation (friction map) for a micro- and mesoscale exemplarily (compare [36]).

It has to be ensured that the friction map consists of an adequate range of pressure and velocity breakpoints so that no friction coefficients outside the fitted map are used during the block simulations on the next coarser length scale. The application of artificial neural networks (ANN) to interpolate between breakpoints like in [34] is found to be working alternatively.

Multi-scale Hysteresis Friction. The combination of the length scale decomposition and the introduced time homogenization leads to a multi-scale friction procedure to compute macroscopic friction features. Figure 10 gives an overview of all required steps of the multi-scale simulations.

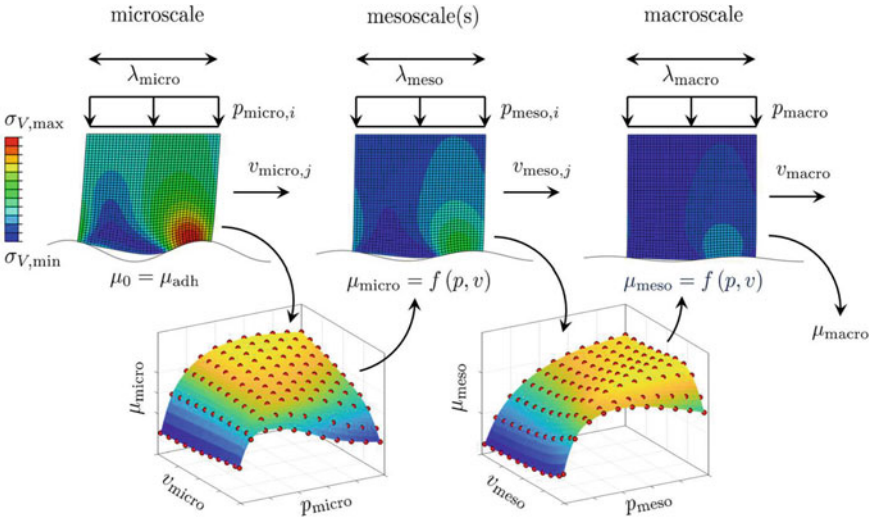

Fig. 10 Schematic outline of the multi-scale friction approach

The multi-scale procedure starts on the microscopic scale, where multiple FE simulations are executed in parallel to compute the interaction between the rubber block and road surface at different loads p_{micro} and sliding velocities v_{micro}. The ranges of p_{micro} and v_{micro} are the output of a preliminary study and may need to be adjusted iteratively. If adhesion friction is considered, the adhesion model described in Sect. 3.1 is applied on the microscale. For every microscale block simulation, the introduced time homogenization adds a breakpoint (see red dots within the diagrams in Fig. 10) into the friction map which is used as a pressure- and velocity-dependent friction law for the mesoscale via spline interpolation. On the mesoscale(s) (depending on the scale identification results), the friction law for the macroscale is formed by performing a sufficient number of block simulations at scale-dependent loads p_{meso} and velocities v_{meso}. Finally, the macroscopic friction coefficient μ_{macro} is gained at the requested boundary conditions p_{macro} and v_{macro} applying the friction map of the coarsest mesoscale as friction law.

Numerical Validation of Multi-scale Approach. The multi-scale approach for hysteresis friction is numerically validated by a simple 2D academic example using two different scales represented by sine waves

$$z\,(x) = \sum_{i=1}^{2} A_i \sin\left(\frac{2\,\pi}{\lambda_i}\,x\right)\,, \tag{9}$$

which is based on [36]. On each scale, a rubber block with the length λ_i is sliding over the corresponding sine wave. The material properties of the rubber block as well as the mesh sizes are mainly taken from [36]. The macroscopic load and slip

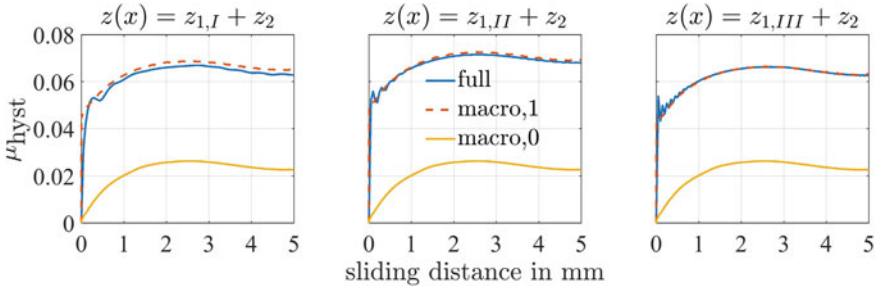

Fig. 11 Numerical validation of the multi-scale approach using two scales

velocity are $1\,^{\text{N}}/_{\text{mm}^2}$ and $500\,^{\text{mm}}/_{\text{s}}$, respectively. The adhesion model is not applied in this example.

The macroscopic wave is described by $z_2(x) = 0.075\,\text{mm} \cdot \sin\left(^{2\pi}/_{5\,\text{mm}}\, x\right)$ with a wavelength of 5 mm. In contrast to [36], three different microscopic scales $z_{1,I}$, $z_{1,II}$ and $z_{1,III}$ with wavelengths of 0.5 mm, 0.2 mm and 0.1 mm are investigated to identify the representative microscale for the predefined macroscale. The ratio between amplitude and wavelength $^{A_i}/_{\lambda_i}$ of each microscopic wave is defined by 0.02. Three diagrams in Fig. 11 display the macroscopic friction coefficients of the reference models (full) with $z_i(x) = z_{1,i}(x) + z_2(x)$, $i = I, II, III$ (from left to right) in comparison to the resulting friction coefficients of the macroscopic scale with ($\mu_{\text{hyst,macro,1}}$) and without ($\mu_{\text{hyst,macro,0}}$) microscopic friction.

The multi-scale approach slightly overestimates the coefficient of friction of the reference model using a wavelength factor between micro- and macroscale of 10. In this example, a representative microscale must be at least larger than 25. Similar findings emerge if the macroscopic load and slip velocity are changed to $0.5\,^{\text{N}}/_{\text{mm}^2}$, $2\,^{\text{N}}/_{\text{mm}^2}$, $100\,^{\text{mm}}/_{\text{s}}$ and $1000\,^{\text{mm}}/_{\text{s}}$. Whereby, the error of the friction coefficient between reference and multi-scale model increases at lower wave length factors if higher load or sliding velocity are applied.

The numerical validation example proves that the quality of the homogenization method depends on the distance between adjacent scales. This fact should be considered within the scale identification to ensure the validity of the multi-scale approach.

4 Pavement Model for Short-Term Loading by Rolling Tires

The FE pavement model, which is presented in this section, is the third important submodel (considering also tire and friction model) that is required to achieve a realistic coupled tire-pavement-interaction description. Thereby, the pavement model has to capture the layered pavement structure, the material properties and the bonding

behavior between the single pavement layers realistically. The layered 3D structure of pavements is modeled by 3D finite elements. The material properties are, therein, described by constitutive formulations, whereby this section focuses on the inelastic behavior of asphalt. Nevertheless, the overall procedure can be adopted to other material formulations (e.g. concrete) as well by implementing the corresponding constitutive formulations. To account for the fact that the single pavement layers are not bonded rigidly to each other, interface elements are included additionally at the boundaries between the single layers [42]. The bonding behavior between the single pavement layers is, then, represented by a viscoelastic, temperature- and (normal) pressure-dependent traction-separation law, which acts as a constitutive formulation for the interface element.

4.1 Constitutive Material Formulation for the Short-Term Behavior of Asphalt

Asphalt Material Model. Asphalt is composed of aggregates, bituminous binder, air voids and additives and, thus, is a heterogeneous material. However, for macroscopic computations, which are done on the scale of the whole pavement structure, asphalt is treated as continuum and its macroscopic material behavior is represented by constitutive formulations. Due to its composition and inner structure, temperature-dependent elastic, viscous and plastic deformation components are observed in asphalt material. To be consistent with the tire model and to account for large deformations that occur in the asphalt in case of ruts, the finite strain constitutive formulation of [50] is applied here to the short-term behavior of asphalt. The formulation bases on the multiplicative split of the deformation gradient

$$\mathbf{F} = \mathbf{F}_{\text{vol}}\,\mathbf{F}_{\text{iso}} = \left(J^{1/3}\mathbf{1}\right)\left(\mathbf{F}^{\text{e}}_{\text{iso}}\,\mathbf{F}^{\text{i}}_{\text{iso}}\right) \tag{10}$$

into a volumetric (index vol) and an isochoric part (index iso). Thereby, the isochoric part consists of an elastic part (index e) and an inelastic part (index i). The Jacobian J represents the volume change ratio related to the reference configuration. The derivative of the strain energy density function Ψ with respect to the left Cauchy-Green tensor $\mathbf{b}$ yields the Kirchhoff stress tensor

$$\boldsymbol{\tau} = J\,\boldsymbol{\sigma} = \boldsymbol{\tau}_{\text{vol}} + \boldsymbol{\tau}_{\text{iso}}\,, \tag{11}$$

which consists of a volumetric and an isochoric part. $\boldsymbol{\sigma}$ is the Cauchy stress tensor, see [19]. The rheology of both parts of the applied asphalt material formulation is illustrated in Fig. 12. Thereby, the volumetric deformation contribution of asphalt (compacted) is assumed to be elastic and is modeled by a spring with bulk modulus κ. The isochoric contribution is modeled by five branches in parallel. The first one is a Neo-Hookean spring with stiffness $C_{10,1}$ and the second branch is a vis-

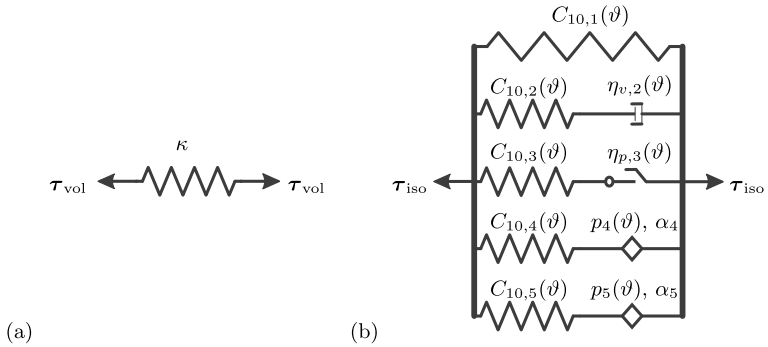

Fig. 12 Rheology of the asphalt material model: **a** volumetric part, **b** isochoric part, see [50]

coelastic Maxwell element with a Neo-Hookean spring $C_{10,2}$ and a dashpot with $\eta_{v,2}$ in series. Rate-independent elastoplastic behavior is represented by the third branch with a Neo-Hookean spring with $C_{10,3}$ and an endochronic frictional element with the plastic parameter $\eta_{p,3}$ in series. The forth and fifth branch capture rate-dependent viscoelastic behavior by fractional Maxwell elements that consist each of a Neo-Hookean spring $C_{10,4}$ and $C_{10,5}$ as well as a fractional element with parameters p_4, α_4 and p_5, α_5, respectively. While p_4 and p_5 are comparable to the viscosity, α_4 and α_5 prescribe the order of the time derivatives.

To capture the temperature-dependent asphalt material response, all parameters depicted in Fig. 12 (except for α_4 and α_5) are monotonous functions of the temperature ϑ. Details of the applied constitutive formulation can be found in [43, 44, 50].

Identification of Material Parameters. The identification of parameters for asphalt mixtures can be done in different ways. First, parameters can be identified based on results of experimental tests of asphalt specimens. Another option is to investigate the behavior of the single asphalt components, especially of the bituminous binder, and to predict the material behavior of asphalt mixtures based on its inner structure and the properties of the constituents. This step can be done e.g. based on microscopic or mesoscopic models of asphalt mixes as demonstrated in chapter "Multi-scale Computational Approaches for Asphalt Pavements under Rolling Tire Load". In this section, the parameters are identified in two steps based on results of repeated load triaxial tests (RLTT) of asphalt specimens that are described in detail in chapter "Experimental Methods for the Mechanical Characterization of Asphalt Concrete at Different Length Scales: Bitumen, Mastic, Mortar and Asphalt Mixture" and in [44].

In the first step of the identification procedure (see [43, 44] for details), parameter sets for the discrete temperature values of the experimental tests are obtained. Therefore, the strain obtained by use of the material model and the strain measured in the experiments for the same loading are compared to each other. The difference between both is minimized by an optimization procedure based on a so-called particle swarm optimization (PSO). By distinguishing between particle and swarm behavior, the PSO approach avoids sticking in single local minima. In the second step of

the identification procedure, monotonously increasing or decreasing functions are adjusted to obtain continuous temperature-dependent parameter functions based on the material parameters at the discrete temperatures from the first step.

4.2 Cohesive Zone Model for Bonding Layers

The bonding behavior between the different asphalt layers influences the overall structural behavior of the pavement essentially. Experimental cyclic tests of the layer bond behavior between two asphalt layers caused by a bituminous emulsion showed that the bonding behavior is not rigid. In contrary, it depends on the loading frequency, the temperature as well as on the present normal pressure [40]. To capture all these dependencies, a viscoelastic cohesive zone model (see [51]) is enhanced to describe the constitutive behavior between bonding traction vector $\mathbf{T}$ and the separation vector $\boldsymbol{\Delta}$ of the interface element. For all normal (tension) and tangential separations (shear) in the interface layer, the bonding traction $\mathbf{T} = \mathbf{T}^{\mathrm{e}} + \mathbf{T}^{\mathrm{v}}$ consists of an elastic and a viscous contribution.

In case that the normal pressure acts on the interface, a contact algorithm that increases the normal contact stiffness is applied in order to minimize the penetration of the two bonded layers [51]. A normal pressure-dependent shear stiffness is obtained in [43] by the implementation of an additional shear traction in the contact algorithm. Further, the corresponding layer bond material parameters are identified based on experimental test results in [43].

4.3 Mechanical ALE FE Pavement Model

Different possibilities are available to model the pavement loaded by a rolling tire. In a classical Lagrangian formulation with respect to the coordinate system $\mathbf{e}_i^{\mathrm{L}}$, which is fixed in space, the tire load is stepwise shifted over the pavement in many time steps, which is numerically expensive and time consuming. An alternative is the application of an ALE formulation. Thereby, a moving reference coordinate system $\mathbf{e}_i^{\mathrm{ALE}}$ is introduced that moves together with the tire through the space, see Fig. 13. In case of steady state rolling tire and pavement, which is homogeneous in longitudinal direction, the deformation state of the pavement becomes steady state as well related to the moved reference frame. This enables time-independent and numerically efficient computations. However, introducing this moving reference frame leads to the fact that the material is no more fixed to the mesh but flows along streamlines through it, which has to be considered in case of inelastic material formulations.

ALE Kinematics. In addition to the initial $\mathcal{B}$ and the current configuration $\Phi(\mathcal{B})$, a reference configuration $\chi(\mathcal{B})$ that includes all rigid body motions is introduced in the ALE kinematics, see Fig. 14. The mapping from initial to current configuration reads then

$$\mathbf{x} = \Phi(\mathbf{X}, t) = \hat{\Phi}(\chi(\mathbf{X}, t)) . \tag{12}$$

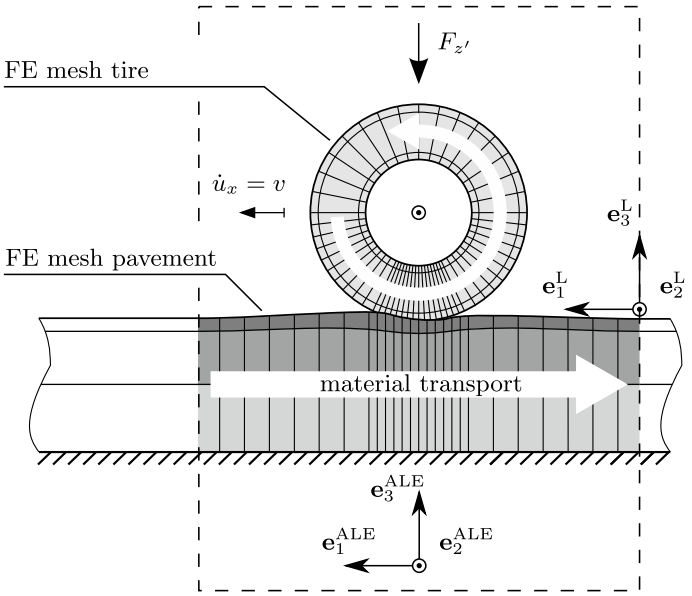

Fig. 13 ALE approach for tire and pavement: FE discretized structures and coordinate systems

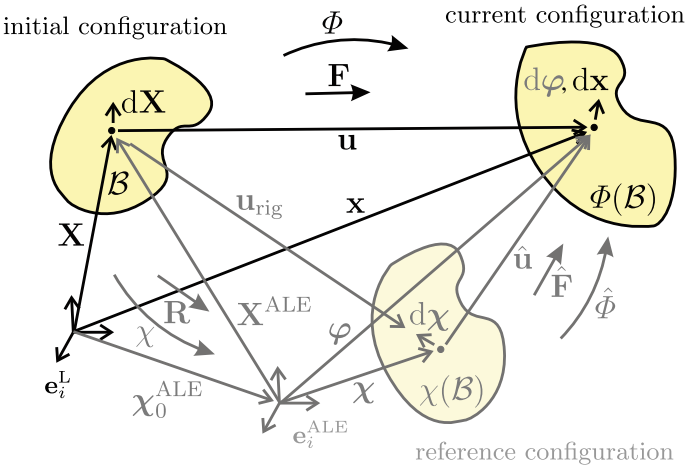

Fig. 14 ALE kinematics

Further, a moving coordinate system $\mathbf{e}_i^{\mathrm{ALE}}$ is used, which describes the reference configuration by the coordinates $\boldsymbol{\chi}$ and the current configuration by coordinates $\boldsymbol{\varphi}$. Thereby, the time-dependent position of the moving coordinate system $\mathbf{e}_i^{\mathrm{ALE}}$ with respect to the fixed Lagrangian coordinate system $\mathbf{e}_i^{\mathrm{L}}$ is given by the vector $\boldsymbol{\chi}_0^{\mathrm{ALE}}(t)$.

Based on the two different introduced coordinate systems, the current position of a point P is given by

$$\mathbf{x} = \mathbf{X} + \mathbf{u} = \boldsymbol{\chi}_{\mathbf{0}}^{\mathrm{ALE}} + \boldsymbol{\varphi} = \boldsymbol{\chi}_{\mathbf{0}}^{\mathrm{ALE}} + \boldsymbol{\chi} + \hat{\mathbf{u}} = \mathbf{X} + \mathbf{u}_{\mathrm{rig}} + \hat{\mathbf{u}} \,. \tag{13}$$

Then, using $\mathbf{x} = \boldsymbol{\chi}_{\mathbf{0}}^{\mathrm{ALE}} + \boldsymbol{\varphi}$ as well as $\partial \boldsymbol{\chi}_{\mathbf{0}}^{\mathrm{ALE}} / \partial \mathbf{X} = 0$, the deformation gradient

$$\mathbf{F} = \frac{\partial \mathbf{x}}{\partial \mathbf{X}} = \mathrm{GRAD}\, \mathbf{x} = \frac{\partial \boldsymbol{\varphi}}{\partial \mathbf{X}} = \frac{\partial \boldsymbol{\varphi}}{\partial \boldsymbol{\chi}} \frac{\partial \boldsymbol{\chi}}{\partial \mathbf{X}} = \hat{\mathbf{F}}\, \mathbf{R} \tag{14}$$

can be split into the rigid body rotations $\mathbf{R}$ from initial to reference configuration with $\det \mathbf{R} = 1$ and into the deformation $\hat{\mathbf{F}}$ from reference to current configuration with the Jacobian $J = \det \mathbf{F} = \det \hat{\mathbf{F}} = \hat{J} > 0$.

Further, the first and second Piola-Kirchhoff stress tensors are defined with respect to the reference frame as

$$\hat{\mathbf{P}} = \hat{J}\, \boldsymbol{\sigma}\, \hat{\mathbf{F}}^{-\mathrm{T}} \quad \text{and} \quad \hat{\mathbf{S}} = \hat{\mathbf{F}}^{-1}\, \hat{\mathbf{P}} \tag{15}$$

in addition to the standard continuum mechanical stress measures of the Cauchy stress tensor $\boldsymbol{\sigma}$, the first Piola-Kirchhoff stress tensor $\mathbf{P} = J\, \boldsymbol{\sigma}\, \mathbf{F}^{-\mathrm{T}}$ and the second Piola-Kirchhoff stress tensor $\mathbf{S} = \mathbf{F}^{-1}\, \mathbf{P}$ (compare e.g. [19]), respectively.

One key issue of ALE kinematics is the material time derivative. Due to the introduced reference frame, the material time derivative of a scalar value f

$$\dot{f} = \left.\frac{\partial f}{\partial t}\right|_{\mathbf{X}} = \left.\frac{\partial f}{\partial t}\right|_{\boldsymbol{\chi}} + \mathrm{Grad}\, f \cdot \mathbf{w} \quad \text{with} \quad \mathrm{Grad}\, f = \frac{\partial f}{\partial \boldsymbol{\chi}}, \quad \mathbf{w} = \left.\frac{\partial \boldsymbol{\chi}}{\partial t}\right|_{\mathbf{X}} \tag{16}$$

is decomposed into a relative and a convective part, see [13]. Thereby, $\mathbf{w}$ is called guiding velocity and corresponds to the velocity with that the material flows through the reference frame. For pavements loaded by steady state rolling tires, the reference frame and coordinate system is moved with the translational tire velocity through the space $\chi_{\mathbf{0}}^{\mathrm{ALE}} = \mathbf{v}_{\mathrm{tire}} \cdot t$. Further, in contrast to the tire, the pavement performs no rigid body motion. Thus, with $\mathbf{u}_{\mathrm{rig,pav}} = 0$ and Eqs. (13) and (16), the guiding velocity of the pavement

$$\mathbf{w}_{\mathrm{pav}} = \left.\frac{\partial \chi}{\partial t}\right|_{\mathbf{X}} = \left.\frac{\partial \left(\mathbf{X} + \mathbf{u}_{\mathrm{rig}} - \chi_{\mathbf{0}}^{\mathrm{ALE}}\right)}{\partial t}\right|_{\mathbf{X}} = -\left.\frac{\partial \chi_{\mathbf{0}}^{\mathrm{ALE}}}{\partial t}\right|_{\mathbf{X}} = -\mathbf{v}_{\mathrm{tire}} \tag{17}$$

is known a priori and is equal to minus one times the translational tire velocity, see [43].

ALE FE Pavement Model. Base for the mechanical FE equation is the balance of momentum in the reference frame given in the weak form

$$\int_{\chi(\mathcal{B})} \hat{\rho}\, \dot{\mathbf{v}} \cdot \boldsymbol{\eta}\, \mathrm{d}\hat{v} + \int_{\chi(\mathcal{B})} \hat{\mathbf{P}} : \mathrm{Grad}\, \boldsymbol{\eta}\, \mathrm{d}\hat{v} = \int_{\chi(\mathcal{B})} \hat{\rho}\, \mathbf{b} \cdot \boldsymbol{\eta}\, \mathrm{d}\hat{v} + \int_{\partial\chi(\mathcal{B})} \hat{\mathbf{T}} \cdot \boldsymbol{\eta}\, \mathrm{d}\hat{a}\,, \tag{18}$$

see [27], whereby $\hat{\rho}$ is the density with respect to the reference frame, $\dot{\mathbf{v}} = \ddot{\mathbf{x}}$ is the material time derivative of the material velocity, $\boldsymbol{\eta}$ are the so-called test functions, $\mathbf{b}$ represents the volume loads and $\hat{\mathbf{T}}$ is the surface traction due to prescribed loads on the body surface as well as due to interfacial traction. It is worth noting that for the steady state case, the inertia term

$$\begin{aligned} \int_{\chi(\mathcal{B})} \hat{\rho}\, \dot{\mathbf{v}} \cdot \boldsymbol{\eta}\, \mathrm{d}\hat{v} = & \int_{\partial\chi(\mathcal{B})} \hat{\rho}\boldsymbol{\eta} \cdot (\mathrm{Grad}\, \boldsymbol{\varphi} \cdot \mathbf{w})\, \mathbf{w} \cdot \hat{\mathbf{n}}\, \mathrm{d}\hat{a} \\ & - \int_{\chi(\mathcal{B})} \hat{\rho}\, (\mathrm{Grad}\, \boldsymbol{\varphi} \cdot \mathbf{w}) \cdot (\mathrm{Grad}\, \boldsymbol{\eta} \cdot \mathbf{w})\, \mathrm{d}\hat{v} \end{aligned} \tag{19}$$

becomes independent of time, as shown in [27].

The standard steps of linearization $\boldsymbol{\varphi}_{(i+1)} = \boldsymbol{\varphi}_{(i)} + \Delta\varphi$ and discretization lead finally to the FE equation for steady state motion

$$\left(\mathbf{K}_{(i)} - \mathbf{W}\right) \Delta\tilde{\varphi} = \hat{\mathbf{f}}_{\mathrm{ext\,(i+1)}} - \hat{\mathbf{f}}_{\sigma\,(i)} - \hat{\mathbf{f}}_{\mathrm{i}\,(i)}\,, \tag{20}$$

whereby the inertia of the material is considered and represented by the time-independent inertia matrix $\mathbf{W}$ and the inertia forces $\hat{\mathbf{f}}_{\mathrm{i}}$, compare [27, 43] for further details. Since the ALE FE equation is independent of time in the steady state case, no time consuming time step algorithm is required for the solution, which is one big advantage of the ALE formulation.

Treatment of Inelastic Materials. Inelastic material formulations typically involve evolution equations of the internal variables $\boldsymbol{\alpha}$, whereby the material time derivative of the internal variables

$$\dot{\boldsymbol{\alpha}} = \left.\frac{\partial \boldsymbol{\alpha}}{\partial t}\right|_{\mathbf{X}} = f(\mathbf{F}, \boldsymbol{\alpha}) \tag{21}$$

depends on the current deformation as well as on the internal variables themselves. In Lagrangian computations, where the material is fixed to the FE mesh, the evolution equation can be solved by numerical time integration

$$\boldsymbol{\alpha}\,(P, t_{n+1}) = f\left(\mathbf{F}\,(P, t_{n+1})\,, \boldsymbol{\alpha}\,(P, t_n)\,, \Delta t\right). \tag{22}$$

In FE implementations, the evolution equation is solved for each integration point. Thus, the material history $\boldsymbol{\alpha}\,(P, t_n)$ of an integration point P is obtained from the internal variables of the same integration point from the previous time step t_n in the Lagrangian frame.

In ALE formulations, the material is no more fixed to the FE mesh but flows, instead, through the reference frame. The evolution equation of the internal variables reads

$$\dot{\boldsymbol{\alpha}} = \left.\frac{\partial \boldsymbol{\alpha}}{\partial t}\right|_{\mathbf{X}} = \left.\frac{\partial \boldsymbol{\alpha}}{\partial t}\right|_{\boldsymbol{\chi}} + \operatorname{Grad}\boldsymbol{\alpha} \cdot \mathbf{w} = f(\mathbf{F}, \boldsymbol{\alpha}) \tag{23}$$

in the ALE frame. Typical solution strategies to solve this evolution equation are unsplit techniques (see e.g. [3]) and operator split techniques, where the solution is split into a Lagrangian and an Eulerian step (see e.g. [9, 49]). For the application to inelastic pavements loaded by steady state rolling tires, the split approach of [49] is adopted in [45] and, further, an approximated unsplit approach is proposed in [43, 45]. The latter one is computationally more efficient as shown in [45]. A validation of the approximated unsplit inelastic ALE approach by comparison to a transient Lagrangian computation is further included in [44]. In the special case of pavements loaded by steady state rolling tires, a pavement material particle takes the time $\Delta t = |\Delta \boldsymbol{\chi}|/|\mathbf{w}|$ to flow with the guiding velocity $\mathbf{w}$ a distance of $\Delta \boldsymbol{\chi}$ along the material streamline through the reference configuration. Then, for the steady state case, where the relative part of the evolution equation given in Eq. (23) vanishes, the material time derivative of the internal variables can be approximated in the unsplit strategy [43, 45] by

$$\dot{\boldsymbol{\alpha}}(P) = \frac{\partial \boldsymbol{\alpha}}{\partial \boldsymbol{\chi}} \cdot \mathbf{w} = f(\mathbf{F}(P), \alpha(P)) \approx \frac{\Delta \boldsymbol{\alpha}(P)}{|\Delta \boldsymbol{\chi}|} \cdot |\mathbf{w}| = \frac{\Delta \boldsymbol{\alpha}(P)}{|\Delta t|}\,. \tag{24}$$

This formulation allows a Lagrangian like numerical time integration for each integration point k

$$\boldsymbol{\alpha}^k = f\left(\mathbf{F}^k, \boldsymbol{\alpha}^{k-1}, \Delta t^k\right). \tag{25}$$

Thereby, the history of the material particle is now taken from the integration point $k-1$ that the particle passed previously and the time that the particle took to pass from integration point $k-1$ to integration point k is obtained from the distance between both points as $\Delta t^k = |\Delta \boldsymbol{\chi}^k|/|\mathbf{w}|$, see Fig. 15. Prerequisite for this method is a regular FE mesh, where the integration points are lying chain-like on the material streamlines in the reference configuration.

4.4 Transient, Thermal FE Pavement Model

The pavement temperature state mainly depends on the climatic conditions. In contrast to the tire, dissipation due to friction and inelastic material behavior in the pavement has a minor effect on the temperature of the pavement and, therefore, is neglected. For the short term of one single tire overrun, it is, thus, assumed that the

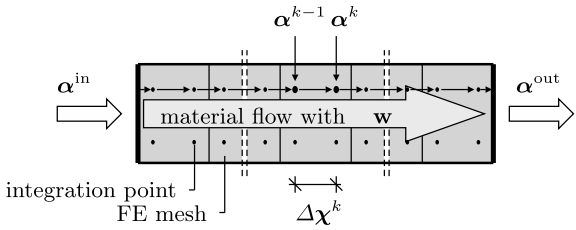

Fig. 15 Transport of the material history [43]

temperature field in the pavement structure is stationary in longitudinal direction. To save computational cost, the pavement temperature field is computed in a thermal 2D FE cross-section model [43]. Base for the thermal computation is the heat balance equation (see e.g. [33]), which leads after linearization and discretization to the FE form

$$\mathbf{C}\,\dot{\tilde{\boldsymbol{\Theta}}} + \mathbf{W}\,\tilde{\boldsymbol{\Theta}} = \tilde{\mathbf{Q}}. \tag{26}$$

Thereby, $\mathbf{C}$ is the heat capacity matrix, $\tilde{\boldsymbol{\Theta}}$ is the nodal temperature vector, $\mathbf{W}$ is the heat conductivity matrix and $\tilde{\mathbf{Q}}$ is the vector of the nodal heat flux. To solve this transient equation, an implicit Euler backward time step algorithm is applied. As time-dependent boundary conditions, temperature (Dirichlet boundary condition) and heat flux (Neumann condition) can be prescribed. The latter one also enables the prescription of convection boundary conditions $q_{\text{c}} = h_{\text{c}} \cdot (\vartheta - \vartheta_{\infty})$ and radiation boundary conditions $q_{\text{r}} = h_{\text{r}}(\vartheta) \cdot (\vartheta - \vartheta_{\text{r}})$ (see e.g. [33]).

4.5 Thermo-mechanical Pavement Model

The coupled thermo-mechanical pavement model consists of the thermal module and the mechanical ALE module [43]. In the thermal module, the time-dependent temperature field of the pavement cross-section is calculated first. Then, the mechanical ALE module can be applied at any prescribed time t^{ALE}. Therefore, it reads the corresponding nodal temperatures $\tilde{\boldsymbol{\Theta}}(t^{\text{ALE}})$ of the thermal cross-section model and transmits them to the equivalent nodes of the mechanical ALE model. Then, the mechanical ALE computation is able to consider the temperature-dependent material properties within the FE bulk and cohesive zone elements.